

# Chemical Linkage and Passivation at Buried Interface for Thermally Stable Inverted Perovskite Solar Cells with Efficiency over 22%

Ying Tan<sup>1</sup>, Xueqing Chang<sup>1</sup>, Jun-Xing Zhong<sup>1</sup>, Wenhui Feng<sup>1</sup>, Meifang Yang<sup>1</sup>, Tian Tian<sup>1</sup>, Li Gong<sup>2</sup> & Wu-Qiang Wu<sup>1\*</sup>

<sup>1</sup>MOE Key Laboratory of Bioinorganic and Synthetic Chemistry, Lehn Institute of Functional Materials, School of Chemistry, Sun Yat-sen University, Guangzhou 510006, <sup>2</sup>Instrumental Analysis Research Center, Sun Yat-sen University, Guangzhou 510275

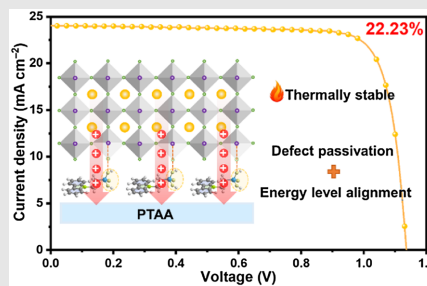
\*Corresponding author: [wuwq36@mail.sysu.edu.cn](mailto:wuwq36@mail.sysu.edu.cn)

Cite this: CCS Chem. **2023**, 5, 1802–1814

DOI: [10.31635/ccschem.022.202202154](https://doi.org/10.31635/ccschem.022.202202154)

Poly[bis(4-phenyl)-(2,4,6-trimethylphenyl)amine] (PTAA) has been developed as one of the most popular hole transport layer (HTL) materials in inverted perovskite solar cells (PSCs). However, the efficiency, thermal stability, and reproducibility of PTAA-based devices are still largely limited by underoptimized chemical interaction, energy level alignment, and contact affinity at the PTAA/perovskite interface. To this end, we introduced a bilateral chemical linker to simultaneously achieve favorable chemical interaction with the PTAA underlayer and form robust coordination bonding with the buried perovskite bottom layer, which beneficially improved the contact affinity, facilitated the hole extraction, well-passivated the interfacial defects, and relieved the nonradiative charge recombination at the HTL/perovskite buried interface. The inverted PSCs modified with interfacial chemical linker exhibited consistently higher power conversion efficiencies and performance reproducibility than that of the PTAA-only devices. Combined with the blade-coated  $\text{FA}_{0.4}\text{MA}_{0.6}\text{PbI}_3$  perovskite layer, a champion efficiency of 22.23% has been achieved, which is one of the highest reported values for the inverted PSCs based on the bilayer HTL. The

targeted device showed enhanced thermal stability under continuous heating at 85 °C owing to suppressed composition segregation with robust interfacial linkage and consolidation. This work offers a new insight towards making efficient, thermally stable, and reproducible perovskite photovoltaics.



An “all-in-one” interlayer was introduced at HTL/perovskite buried interface to achieve favorable energy level alignment with underlying PTAA and form robust coordination bonding with adjacent perovskite for maximized interfacial hole extraction and suppressed interfacial charge recombination. A champion efficiency of 22.23% was achieved for the bilayered HTL-based inverted PSCs, accompanied by excellent reproducibility and extended lifespan (>2000 h) in ambient air and 85 °C thermal stress.

**Keywords:** perovskite solar cells, hole extraction, charge recombination, defect passivation, thermal stability

## Introduction

Over the past decade, metal halide perovskite solar cells (PSCs) have attracted intensive research attention owing to their fascinating advantages, including high efficiency, low cost, and solution processability, rendering them one of the most promising next-generation photovoltaic technologies.<sup>1–4</sup> With strenuous efforts made on composition optimization, crystallization regulation, interface engineering, and device architecture design, the power conversion efficiencies (PCEs) of PSCs have been progressively lifted and certified to be as high as 25.7%, which is already on par with or even surpassing their silicon-based competitors.<sup>5</sup> Among various types of PSCs, the inverted devices with a *p-i-n* configuration are of particular interest due to their low-temperature fabrication processability, which is compatible for use in flexible or tandem solar cells with greater practical application value.<sup>6,7</sup>

For the inverted PSCs, the *p*-type hole transport layer (HTL) served as a hole-selective contact between the transparent conducting oxide substrate and the perovskite layer, which is responsible for extracting the photo-generated holes and inevitably affects the crystallization kinetics of the adjacent perovskite layer. Among the various types of reported HTLs, the poly[bis(4-phenyl)-(2,4,6-trimethylphenyl)amine] (PTAA) has been demonstrated as one of the most popular and successful HTL materials in the inverted PSCs.<sup>8–11</sup> Though promising, there is still a plenty of room to further optimize the PTAA-based PSCs, especially considering several fatal drawbacks that significantly limit the enhancement of device performance. First, the PTAA HTL is notorious for its hydrophobic property, which shows poor wettability to the perovskite ink, thus increasing the difficulties of realizing uniform coating of the perovskite layer on top of the entire PTAA layer, resulting in poor interfacial contact.<sup>12</sup> Second, the PTAA molecules have negligible interaction with perovskites, which minimally affect the crystallization kinetics of perovskite films. Third, it has been reported that the defective PTAA/perovskite interface with a large number of randomly oriented nanocrystals cause serious interfacial nonradiative recombination, thus significantly limiting the device performance, especially the open-circuit voltage ( $V_{OC}$ ).<sup>13</sup> Finally, the energy-level alignment between PTAA and the perovskite is still underoptimized, leading to moderate hole extraction at the HTL/perovskite interface.<sup>14</sup> Modifying the hydrophobic PTAA surface with hydrophilic molecules<sup>15–19</sup> or improving the electrical properties of the PTAA layer via doping<sup>20–23</sup> have been developed to partially solve the above-mentioned problems. However, the reported strategies do not always work effectively, and the repetition of device performance is largely affected by the PTAA materials of different molecular weights.<sup>24,25</sup> In addition, thermally stable PTAA-based PSCs operating

at 85 °C for a long time are rarely reported, considering the heat-resistant capability of polymer-based HTL is not that good, and the fixation of intact perovskites is not ideal. Hence, it is highly desirable and of great significance to explore a universal and effective way to modify the PTAA/perovskite interface to maximize the interfacial charge extraction and minimize the interfacial charge recombination while simultaneously enhancing the thermal stability of resultant devices.

In this work, we introduced an “all-in-one” [2-(9H-carbazol-9-yl)ethyl]phosphonic acid (2PACz) interlayer between the PTAA and perovskite layer, which could achieve favorable energy-level alignment with underlying PTAA and form robust coordination bonding with adjacent perovskite for facilitated interfacial hole extraction and suppressed interfacial charge recombination. Encouragingly, an impressive efficiency over 22.23% with a high  $V_{OC}$  of 1.14 V and negligible photocurrent density–photovoltage ( $J-V$ ) hysteresis was obtained for the inverted PSCs modified with 2PACz interlayer. This, to the best of our knowledge, is one of the highest reported values for the bilayered HTL-based inverted PSCs. In addition, the devices without encapsulation exhibited extended lifespan (>2000 h) against ambient storage and thermal stress.

## Experimental Methods

### Materials

Formamidinium iodide (99.99%), methylammonium iodide (99.99%), and methyl ammonium bromide (99.99%) were purchased from GreatCell Solar Limited (Australia). *N,N*-dimethylmethanamide (DMF, 99.8%), dimethyl-sulfoxide (DMSO, 99.9%), chlorobenzene (CB, 99.8%), and bathocuproine (BCP) were obtained from Sigma-Aldrich (Shanghai, China). PTAA (99%, Mw < 6000), lead bromide (PbBr<sub>2</sub>, 99%) and C<sub>60</sub> was purchased from Xi'an Polymer Light Technology Corp. (Xi'an, China). CsI (99.999%) and PbI<sub>2</sub> (99.999%) were obtained from Alfa Aesar (Shanghai, China). 2PACz was purchased from TCI (Shanghai, China) Development Co., Ltd. All chemicals were employed as received without further modification.

### Perovskite precursor preparation

For the Cs<sub>0.05</sub>(FA<sub>0.83</sub>MA<sub>0.17</sub>)<sub>0.95</sub>Pb(I<sub>0.83</sub>Br<sub>0.17</sub>)<sub>3</sub> perovskite, the precursor solution (1.5 M) was prepared in mixed solvents of DMF and DMSO with a volume ratio of 4:1.

For the FA<sub>0.4</sub>MA<sub>0.6</sub>PbI<sub>3</sub> perovskite, the precursor solution (1.2 M) was prepared in 2-ME solution. Before use, small amounts of additives, that is, methylammonium hypophosphite (0.15 wt %) and L- $\alpha$ -phosphatidylcholine (0.05 wt %), were incorporated to achieve uniform coating of the perovskite film.

## Device fabrication

The PSCs were fabricated with an inverted structure of indium tin oxide (ITO)/PTAA with or without 2PACz/perovskite/C<sub>60</sub>/BCP/Cu. The ITO substrates were cleaned by sequential ultrasonication in deionized water, acetone, and isopropanol, respectively, and then dried in the oven. Next, the substrate underwent UV ozone treatment for 20 min. PTAA (5.0 mg mL<sup>-1</sup> in CB) was dynamically spin-coated onto ITO glass at 5000 rpm for 30 s and then annealed at 100 °C for 10 min. For the device with 2PACz interlayer, the 2PACz solution (10 mg mL<sup>-1</sup> in DMF) was dynamically spin-coated on top of the PTAA layer at 5000 rpm for 30 s and then annealed at 100 °C for 5 min. Then, the perovskite ink was spin-coated onto the ITO/HTL substrates at 2000 rpm for 10 s and 6000 rpm for 30 s, in which 200 μL of CB was dropped on the spinning substrate 15 s prior to the end of the second step. The substrates were then annealed on hotplate at 100 °C for 10 min to obtain crystalline perovskite film. For the FA<sub>0.4</sub>MA<sub>0.6</sub>PbI<sub>3</sub> devices, the precursor solution was blade-coated onto the ITO/HTL substrates with a gap of 100 μm at a blade speed of 10 mm s<sup>-1</sup>. The N<sub>2</sub> knife worked at 0.2 MPa during blade-coating. 8 μL perovskite ink was used for each coating, followed by thermal annealing at 100 °C for 10 min to obtain the perovskite film. Finally, 20 nm C<sub>60</sub>, 7 nm BCP and 80 nm Cu were sequentially thermally evaporated on top of the perovskite films to complete the device.

## Characterization

The Fourier transform infrared (FT-IR) spectrum was measured with a PerkinElmer Frontier FT-IR spectrometer (PerkinElmer, United States) in the range 4000–400 cm<sup>-1</sup>. The surface wettability was measured using an optical contact angle analyzer (KRÜSS-DSA100, Kruss, Germany). The X-ray diffraction (XRD) pattern was obtained from a Miniflex600 X-ray diffractometer (Rigaku, Japan). The morphological features of the samples were characterized using a field emission scanning electron microscope (SEM, Hitachi-SU8010, Hitachi, Japan). Conductive atomic force microscopy (c-AFM) measurements were performed on a scanning probe microscope (Bruker Dimension Fastscan, Bruker, Germany). The Raman spectrum was measured with microconfocal Raman spectrometer (InVia, United Kingdom). J-V characteristics of the PSCs were measured using a Keithley 2400 SourceMeter under the simulated AM1.5G irradiation generated by the Oriel Sol3A Class AAA Solar simulator based on Xenon lamps. The light intensity was calibrated by a silicon reference cell equipped with a SCHOTT visible color KG5 glass filter (Newport 91150V). Nonreflective shadow masks with an aperture of 0.08 cm<sup>2</sup> were used to define the active working areas of the PSCs. For the space-charge limited current (SCLC) test, the J-V characteristics

were measured using a CH Instruments CHI660 electrochemical (ChenHua, China) workstation in a shield box with a structure of ITO/HTL/perovskite/Spiro-OMeTAD/Cu, where the HTL is PTAA or PTAA/2PACz. External quantum efficiency (EQE) was measured by the solar cell quantum efficiency measurement system (SCS10, Zolix Instruments Co., Ltd., China). An Edinburgh Instruments Ltd FLSP980 (Edinburgh, United Kingdom) was used to test the steady-state photoluminescence (PL) and time-resolved photoluminescence (TRPL) with a pulsed excitation laser of 400 nm. The electrochemical impedance spectroscopy (EIS) analysis was carried out using an electrochemical workstation (Zahner Zennium, Zahner, Germany) with the frequency range from 10 Hz to 1 MHz without illumination and under an applied bias of -0.8 V. Transient absorption was measured by a regeneratively amplified Ti: sapphire laser source (Coherent Legend, 800 nm, 150 fs, 5 mJ per pulse, and 1 kHz repetition rate) and Helios (Ultrafast Systems LLC, United States) spectrometer.

## Results and Discussion

In a preliminary study, the PTAA materials with a molecular weight less than 6 kDa and Cs<sub>0.05</sub>(FA<sub>0.83</sub>MA<sub>0.17</sub>)<sub>0.95</sub>Pb(I<sub>0.83</sub>Br<sub>0.17</sub>)<sub>3</sub> perovskites were employed to assemble inverted PSCs. The polymeric PTAA molecule has a poly-triarylamine skeleton (Figure 1a), and the hydrophobicity of solution-processed PTAA film is heavily dependent on the aggregation degree and molecular weight of PTAA. Similar to the dilemma commonly encountered by other researchers, the perovskite film deposited on pristine PTAA film showed very poor surface coverage owing to the poor wettability of the perovskite ink on the hydrophobic surface of PTAA film. Treating the PTAA surface with DMF solvent only partially solved the problem.<sup>15,20</sup> The resultant perovskite film still showcased incomplete surface coverage, which is not desirable for large-scale deployment of PSCs. To this end, a thin layer of 2PACz, featuring a structure of carbazole and phosphonic acid (PA) group connected by a C<sub>2</sub>H<sub>4</sub> chain (Figure 1b), has been deposited on a PTAA layer, prior to the perovskite layer deposition. We can obtain the uniform coating and full surface coverage of perovskite film on PTAA/2PACz substrates (Supporting Information Figure S1), which can be attributed to the enhanced wettability of the PTAA surface with 2PACz modification, as is evidenced by the decreased contact angle from 35.7° to 13.1° (Figure 1c,d). In this case, 2PACz with polar and hydrophilic PA groups plays a critical role in improving the contact affinity between HTL substrate and perovskite ink. In general, enhanced wettability of HTL is a result of higher nucleation density of perovskites, which is conducive to the densification growth of perovskite film with improved quality and better coverage.<sup>19</sup> Atomic force microscopy (AFM)

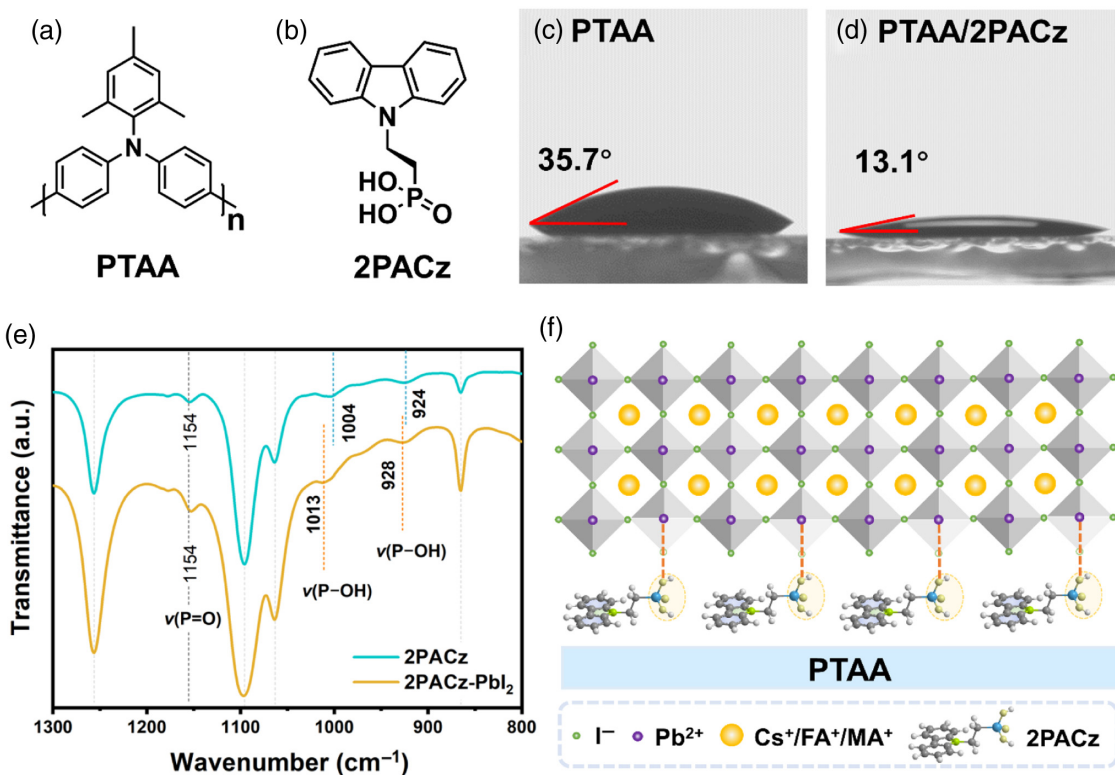


**Figure 1** | Chemical structure of (a) PTAA and (b) 2PACz. Contact angle images for a droplet of perovskite precursor on (c) PTAA and (d) PTAA/2PACz. (e) FT-IR spectra of pristine 2PACz and 2PACz-PbI<sub>2</sub> blend. (f) Schematic illustration of chemical interaction and defect passivation of PTAA/perovskite buried interface by 2PACz molecules.

and scanning electron microscopy (SEM) were also used to investigate the surface topography of the PTAA films with or without 2PACz modification. The 2PACz-treated PTAA layer exhibited a smoother surface than the pristine PTAA film, which was manifested by the smaller root-mean-square value (i.e. 2.66 vs 4.09 nm, *Supporting Information Figure S2*). This result was also consistent with the morphological observation from SEM images (*Supporting Information Figure S3*). Reduced surface roughness of HTL is highly desirable in planar heterojunction PSCs, which is beneficial to improve the interfacial contact between HTL and perovskite layer, thus ensuring high device performance.<sup>17,26</sup>

The functions of 2PACz interlayer far exceed enhancing the wettability of the HTL surface and improving the HTL/perovskite contact affinity. It is anticipated that the 2PACz containing a carbazole structure and PA groups is able to chemically interact with both underlying PTAA and upper perovskite layer. The interaction between 2PACz and PTAA has been investigated by Raman spectroscopy (*Supporting Information Figure S4*), which has been widely utilized to investigate the potential chemical interaction between different molecules with specific functional groups and/or organic moieties.<sup>27–29</sup> For the PTAA sample, the peak located at 1293 cm<sup>-1</sup> corresponded to the C-N bond stretching vibration of the triphenylamine structure.

For the 2PACz sample, the peaks located at 1214 and 1233 cm<sup>-1</sup> corresponded to the stretching vibration of C=C bond of the disubstituted benzene ring, and the peaks located at 1230 and 1356 cm<sup>-1</sup> corresponded to the C-N bond stretching vibration of the pyridine ring. Obviously, considerable red-shifts of these Raman peaks were observed in the PTAA-2PACz sample, indicating decreased electron cloud density of the corresponding chemical bonds. It can be interpreted that such electron delocalization effect is caused by the weak chemical interaction between PTAA and 2PACz molecules. Considering the relatively weak interaction between 2PACz and the underlying PTAA layer, one could assume that the 2PACz can be partially washed away during the subsequent deposition of the perovskite layer. We adopted AFM step height measurement to determine the thickness of different HTLs and their combinations. As a result, the thickness of the pristine PTAA HTL layer was determined to be ~8 nm, and the thickness of the PTAA/2PACz bilayered HTL after DMF washing was determined to be ~11 nm (*Supporting Information Figure S5*). Hence, one could conclude that the thickness of 2PACz interlayer between the PTAA layer and perovskite layer is approximately 3 nm. 2PACz itself is a *p*-type material, which has an excellent hole extraction capability.<sup>11,30,31</sup> It is reported that the hole mobility of the 2PACz derivatives was almost

one magnitude higher than that of the undoped PTAA materials.<sup>25,32</sup> In our case, the conductivity of the PTAA and PTAA/2PACz HTLs was evaluated by the SCLC technique, and the device structure of ITO/HTL/Cu was used for characterization (*Supporting Information Figure S6*). Typically, the direct current (DC) conductivity ( $\sigma_0$ ) can be calculated from the slope of the  $\log(J-V)$  plot in the ohmic region (*Supporting Information Figure S6b*) by using the equation:<sup>33</sup>

$$J = \sigma_0 (A/d) V \quad (1)$$

where  $A$  is the area of sample ( $0.08\text{ cm}^2$ ) and  $d$  is the thickness of sample (i.e.  $8\text{ nm}$  for PTAA and  $11\text{ nm}$  for PTAA/2PACz), respectively. As a result, the conductivity of PTAA/2PACz HTL is  $1.35 \times 10^{-5}\text{ S cm}^{-1}$ , which is much higher than that of the pristine PTAA HTL ( $9.95 \times 10^{-6}\text{ S cm}^{-1}$ ). The increased conductivity of bilayered HTL can be attributed to the intrinsically high hole mobility of 2PACz itself, as well as reduced hole injection barrier due to more matched interfacial energy level alignment between PTAA and 2PACz.<sup>27,34</sup> The pristine 2PACz also showcased the vibration signals for P-OH groups at  $1004$  and  $924\text{ cm}^{-1}$ . Mixing the 2PACz with  $\text{PbI}_2$  red-shifted the vibration peaks of P-OH groups to  $1013$  and  $928\text{ cm}^{-1}$ , respectively (Figure 1e). Such an obvious shift of FT-IR peaks could be ascribed to the chemical interaction between PA groups and metal halides, which is consistent with the previous reports.<sup>30,35-37</sup> Specifically, 2PACz could function as a Lewis base due to its PA groups, which could form coordination bonds with the empty  $6p$  orbital of the  $\text{Pb}^{2+}$  in the perovskites.<sup>38,39</sup> As schematically illustrated in Figure 1f, the 2PACz molecule serves as a two-way bridge to chemically couple with both PTAA and perovskite, which can modify the surface properties of PTAA and passivate the defects at buried HTL/perovskite interface via robust coordination bonding, which is beneficial to facilitate the interfacial charge extraction and suppress the interfacial charge recombination.

The improved contact affinity and chemical interaction effect will be in favor of forming high-quality perovskite films with improved crystallinity and optimized morphologies.<sup>40</sup> We then investigated the effect of the 2PACz modification layer on the crystallinity and morphologies of perovskite films. The 2PACz interfacial linkage slightly enhanced the crystallinity of perovskite film without changing the crystal structure of the perovskite films (*Supporting Information Figure S7*). Compared with the PTAA-based sample, the perovskite film grown on PTAA/2PACz substrate was smoother and the grain size was relatively larger (*Supporting Information Figure S8*). In general, the improved wettability of PTAA/2PACz substrate to the perovskite solution should result in higher nucleation density and thus smaller grain sizes. Herein, the abnormally enlarged grain sizes of the perovskite film

deposited on PTAA/2PACz substrate can be explained by the following reasons. On one hand, some portion of 2PACz could be washed into the perovskite layer and chemically interacted with the perovskites, namely, by forming coordination bonding between PA groups and metal ions, which can retard the fast reaction between metal halides and organic ammonium halides, thus slowing down the crystallization process and ensuring the growth of large grains.<sup>37,41</sup> On the other hand, the smoother surface of underlying PTAA/2PACz substrate enabled fast mass transfer process, such as grain boundary movement, which is beneficial to facilitate the Ostwald ripening process, thus resulting in the formation of perovskite films with large grains.<sup>42</sup> The smooth surface is favorable to the subsequent coating of a uniform electron transport layer (ETL), and the large grains are characterized by less grain boundaries and reduced defect densities, which are all advantageous for achieving better device performance.

We fabricated the inverted PSCs with a device architecture of ITO/HTL/perovskite/ $\text{C}_{60}$ /BCP/Cu, in which the HTL is either pristine PTAA or bilayered PTAA/2PACz (Figure 2a). The cross-sectional SEM images of the corresponding devices are displayed in *Supporting Information Figure S9*, which shows that the thickness of perovskite film is  $\sim 500\text{ nm}$  for both devices. One can observe better interfacial contact junctions at PTAA/2PACz-based devices, showcasing columnar-like perovskite grains tightly connecting with both HTL and ETL (*Supporting Information Figure S9b*), which is helpful for boosting carrier extraction and transport throughout the monolithic device.<sup>17</sup> Figure 2b shows the  $J-V$  curves of the PTAA and PTAA/2PACz-based PSCs fabricated with  $\text{Cs}_{0.05}(\text{FA}_{0.83}\text{MA}_{0.17})_{0.95}\text{Pb}(\text{I}_{0.83}\text{Br}_{0.17})_3$  perovskite films. The corresponding photovoltaic parameters, such as short-circuit photocurrent density ( $J_{\text{SC}}$ ), open-circuit photovoltage ( $V_{\text{OC}}$ ), fill factor (FF), and PCE, are summarized in Table 1. Relative to PTAA-based PSCs, all the photovoltaic parameters of the PTAA/2PACz-based devices improved dramatically, boosting the PCE from 18.14% to 20.05%, accompanied by a negligible  $J-V$  hysteresis with remarkably reduced hysteresis index (*Supporting Information Figure S10* and *Table S1*). Such a performance enhancement can be ascribed to the synergistic roles of facilitated hole extraction and suppressed charge recombination at HTL/perovskite buried interface with 2PACz modification, which will be discussed in the following. The alleviated  $J-V$  hysteresis can be attributed to the optimized carrier dynamics with reduced charge accumulation at the HTL/perovskite interface.<sup>43</sup> In addition, PTAA/2PACz-based devices had greatly reduced leakage current densities as compared to the PTAA-based PSCs (*Supporting Information Figure S11*), suggesting the compactness of both the bilayered HTL film and perovskite layer.<sup>44</sup> The EQE was measured to check the reliability of the enhanced photocurrent (*Supporting Information Figure S12*), and the PTAA/2PACz-based device exhibited

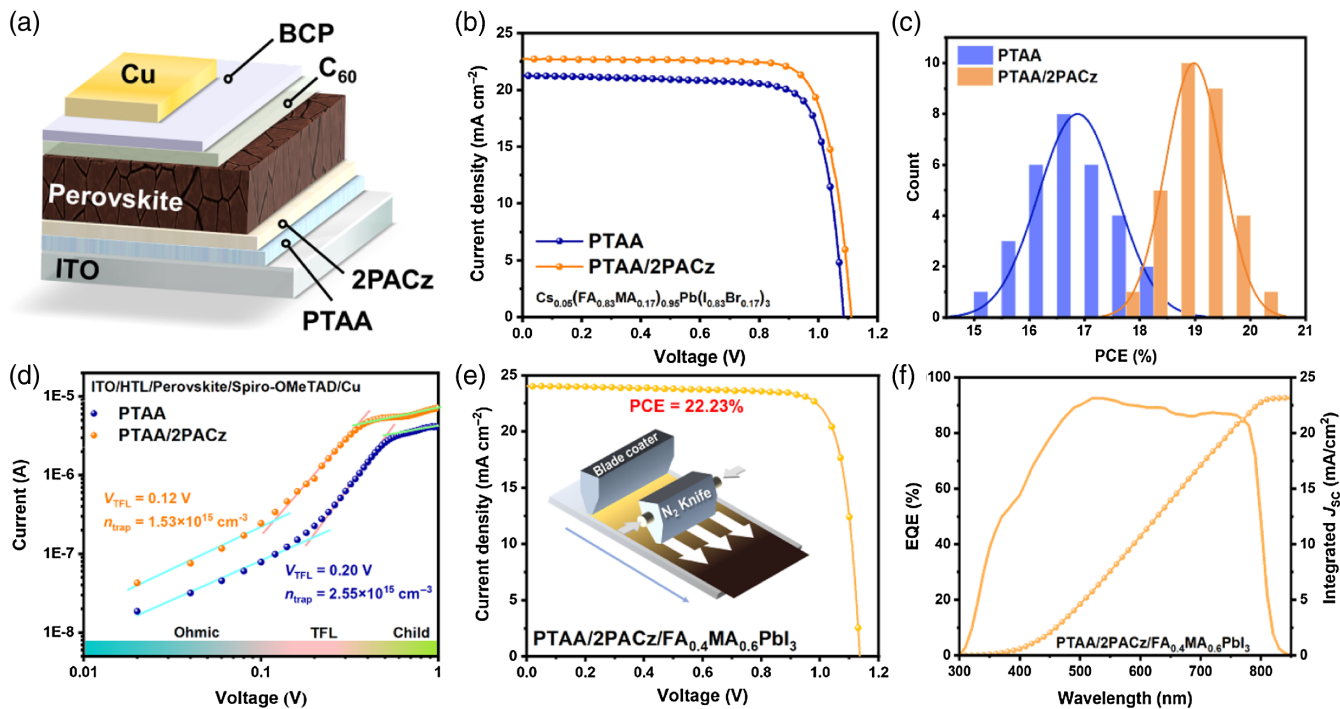


**Figure 2 |** (a) Schematic illustration of inverted PSC with a device architecture of ITO/PTAA/2PACz/perovskite/C<sub>60</sub>/BCP/Cu. (b) J-V characteristics and (c) PCE histogram of Cs<sub>0.05</sub>(FA<sub>0.83</sub>MA<sub>0.17</sub>)<sub>0.95</sub>Pb(I<sub>0.83</sub>Br<sub>0.17</sub>)<sub>3</sub>-based PSCs fabricated with or without 2PACz interlayer. (d) J-V characteristics of the hole-only devices (as indicated) measured under dark conditions. (e) J-V curve and (f) EQE spectrum and integrated J<sub>SC</sub> value of the champion blade-coated PSC based on PTAA/2PACz HTL and FA<sub>0.4</sub>MA<sub>0.6</sub>PbI<sub>3</sub> perovskite film.

higher EQE values over the wavelength region from 380 to 760 nm, relative to the PTAA-based PSC, which is in good consistency with the J-V measurement. Supporting Information Figure S13 presents the steady output of photocurrent density and PCE as a function of time for the PSCs operating at the maximum power point as indicated. A stabilized PCE of 19.36% is achieved for the device based on PTAA/2PACz HTL, which is higher than that of its PTAA-based counterpart. The PTAA/2PACz-based PSCs exhibited better PCE reproducibility than the reference PTAA-only ones (Figure 2c). Specifically, more than 46% of PTAA/2PACz-based devices had PCEs over 19%, while only 6.7% of PTAA-based PSCs showed PCEs over 18%. The outstanding reproducibility of device performance validates the effectiveness of employing bilayered PTAA/2PACz HTL.

Typically, the enhancement of  $V_{OC}$  by ~50 mV for the PTAA/2PACz-based PSCs can be mainly attributed to the reduced defect densities and suppressed trap-assisted recombination within the devices and/or at relevant interfaces. The defect state densities of the perovskite films were determined by measuring the J-V curves of the hole-only devices under dark conditions. The trap-filled limit voltage ( $V_{TFL}$ ) can be obtained and the defect state density ( $N_t$ ) can be calculated according to the following equation:<sup>45</sup>

$$N_t = \frac{2\epsilon\epsilon_0 V_{TFL}}{qL^2} \quad (2)$$

where  $\epsilon_0$  represents the vacuum dielectric constant,  $\epsilon$  is the relative permittivity of perovskite (~28.8 for Cs<sub>0.05</sub>(FA<sub>0.83</sub>MA<sub>0.17</sub>)<sub>0.95</sub>Pb(I<sub>0.83</sub>Br<sub>0.17</sub>)<sub>3</sub> perovskite),<sup>46</sup>  $L$  is the thickness of perovskite film (~500 nm, Supporting Information Figure S9), and  $q$  denotes the elementary charge. As compared to the PTAA-based device ( $V_{TFL} = 0.20$  V,  $N_t = 2.55 \times 10^{15}$  cm<sup>-3</sup>), the PTAA/2PACz-based device achieved a decreased  $V_{TFL}$  of 0.12 V and a reduced  $N_t$  of  $1.53 \times 10^{15}$  cm<sup>-3</sup> (Figure 2d). The reduction of defect density can be ascribed to improved quality of the perovskite bulk film and robust passivation of interfacial imperfections at the buried HTL/perovskite interface with 2PACz modification. EIS was employed to study the charge recombination behavior within the devices. By fitting the Nyquist plots with the as-indicated equivalent circuit, one can conclude the targeted device with 2PACz passivation had the smaller series resistance ( $R_s$ ) and higher recombination resistance ( $R_{rec}$ ) (Supporting Information Figure S14), further verifying better charge transfer property and largely suppressed charge recombination behavior.

We also combined the PTAA/2PACz HTL with the blade-coated FA<sub>0.4</sub>MA<sub>0.6</sub>PbI<sub>3</sub> perovskite for the sake of

**Table 1 | Summarized Photovoltaic Parameters of the Inverted PSCs Based on PTAA or PTAA-2PACz HTL Measured under AM 1.5G One Sun Illumination (100 mW cm<sup>-2</sup>)**

Devices	Perovskites	V <sub>OC</sub> (V)	J <sub>SC</sub> (mA cm <sup>-2</sup> )	FF (%)	PCE (%)	Average PCE <sup>a</sup> (%)
PTAA	Cs <sub>0.05</sub> (FA <sub>0.83</sub> MA <sub>0.17</sub> ) <sub>0.95</sub>	1.09	21.26	78.3	18.14	16.88 ± 0.69
PTAA/2PACz	Pb(I <sub>0.83</sub> Br <sub>0.17</sub> ) <sub>3</sub>	1.13	22.76	78.7	20.05	18.98 ± 0.50
PTAA/2PACz	FA <sub>0.4</sub> MA <sub>0.6</sub> PbI <sub>3</sub>	1.14	24.05	81.1	22.23	/

<sup>a</sup> The average PCE was calculated from a batch of 30 devices for each condition.

further improving the device performance. A champion PCE of 22.23% was achieved, accompanied by a J<sub>SC</sub> of 24.05 mA cm<sup>-2</sup>, a V<sub>OC</sub> of 1.14 V, and a FF of 81.1% (Figure 2e, an illumination area of 0.04 cm<sup>2</sup>). We measured the J-V curves of the champion device under different scanning directions (Supporting Information Figure S15), which showed negligible J-V hysteresis. The EQE spectrum of the champion device showed an integrated J<sub>SC</sub> of 23.16 mA cm<sup>-2</sup> (Figure 2f), which is in good consistency with the J<sub>SC</sub> obtained from J-V curves, showing a discrepancy of only 3.7%. This result again manifests the versatility and effectiveness of 2PACz modification at the buried HTL/perovskite interface to improve the efficiency and stability of inverted PSCs, regardless of perovskite compositions or deposition techniques.

2PACz is capable of serving as an independent HTL in inverted PSCs due to its good hole mobility and sufficiently low highest occupied molecular orbital level (~5.6 eV),<sup>30</sup> which could match well with most of the commonly used perovskite compositions.<sup>30,47–52</sup> However, there is still a considerably large energy barrier from 2PACz to ITO glass with a work function of ~4.8 eV, unless the 2PACz layer is thin enough to minimize the interfacial charge transfer resistance. In the case of bilayered PTAA/2PACz HTL, more matched energy level alignment and cascaded hole transfer can be achieved at the ITO/HTL/perovskite interface (Figure 3a),<sup>30,52</sup> which is beneficial to reduce the energy loss and facilitate the hole extraction and collection.<sup>19,53,54</sup>

We investigated the effect of 2PACz interfacial linkage on the carrier transfer and recombination dynamics at the HTL/perovskite interface.<sup>27</sup> Steady-state and time-resolved PL measurement were conducted for the Cs<sub>0.05</sub>(FA<sub>0.83</sub>MA<sub>0.17</sub>)<sub>0.95</sub>Pb(I<sub>0.83</sub>Br<sub>0.17</sub>)<sub>3</sub> perovskite film deposited on different substrates. The glass/perovskite sample exhibited the strongest PL intensity at 759 nm while diminished PL intensity was observed with the perovskite film stacked on PTAA or PTAA/2PACz substrate. The most significant PL quenching has been attained for the PTAA/2PACz-based sample (Figure 3b), suggesting the most efficient hole extraction from perovskite to bilayered HTL.<sup>55</sup> Similarly, the device modified

with 2PACz showcased a shorter TRPL decay lifetime (184.17 ns) than that of the device with pristine PTAA (220.05 ns), again verifying that the 2PACz interlayer effectively accelerated the hole-extraction at the HTL/perovskite interface (Figure 3c and Supporting Information Table S2).<sup>56,57</sup>

We then further visualized and quantified the boosted hole extraction in PTAA/2PACz-based devices. c-AFM measurement was carried out to characterize the hole extraction capabilities of different HTL/perovskite stacks with or without 2PACz modification (Figure 3d). The hole current collected from the surface of perovskite film remarkably increased for the PTAA/2PACz-based sample (Figure 3e,f), proving the beneficial role of 2PACz in boosting the hole extraction and collection,<sup>58</sup> which is consistent with the above PL and TRPL characterization and analysis. Moreover, the hole mobilities of perovskite films deposited on different HTLs can be quantified by SCLC measurement shown in Figure 2d.<sup>21,42</sup> As a result, the hole mobility of the perovskite film grown on PTAA/2PACz HTL ( $4.86 \times 10^{-4}$  cm<sup>2</sup> V<sup>-1</sup> s<sup>-1</sup>) is ~5-fold higher than that of the perovskite film deposited on PTAA HTL ( $1.05 \times 10^{-4}$  cm<sup>2</sup> V<sup>-1</sup> s<sup>-1</sup>), owing to the improved quality and reduced defects for the former. Note, the hole mobility of perovskite film is nearly one order of magnitude higher than that of HTL, which in turn suggests the necessity and significance of improving the hole conducting capability of HTL itself for ensuring efficient interfacial hole extraction and balancing the charge collection within the devices.<sup>54,59</sup> In our case, the concurrent enhancement of hole mobilities for both HTL and perovskite film jointly contribute to the facilitated hole extraction at buried interface in inverted PSCs.

We employed femtosecond transient absorption (fs-TA) spectroscopy to analyze the ultrafast carrier transfer dynamics of ITO/HTL/perovskite stacked films on the picosecond timescale (Figure 4a).<sup>60</sup> The contour plots of the TA spectrum for both devices exhibited a distinct ground-state bleaching (GSB) peak around 760 nm. Specifically, more promptly faded GBS signal was observed in the PTAA/2PACz/perovskite stack, representing a faster hole extraction rate from the conduction band of perovskite film to adjacent HTL contact

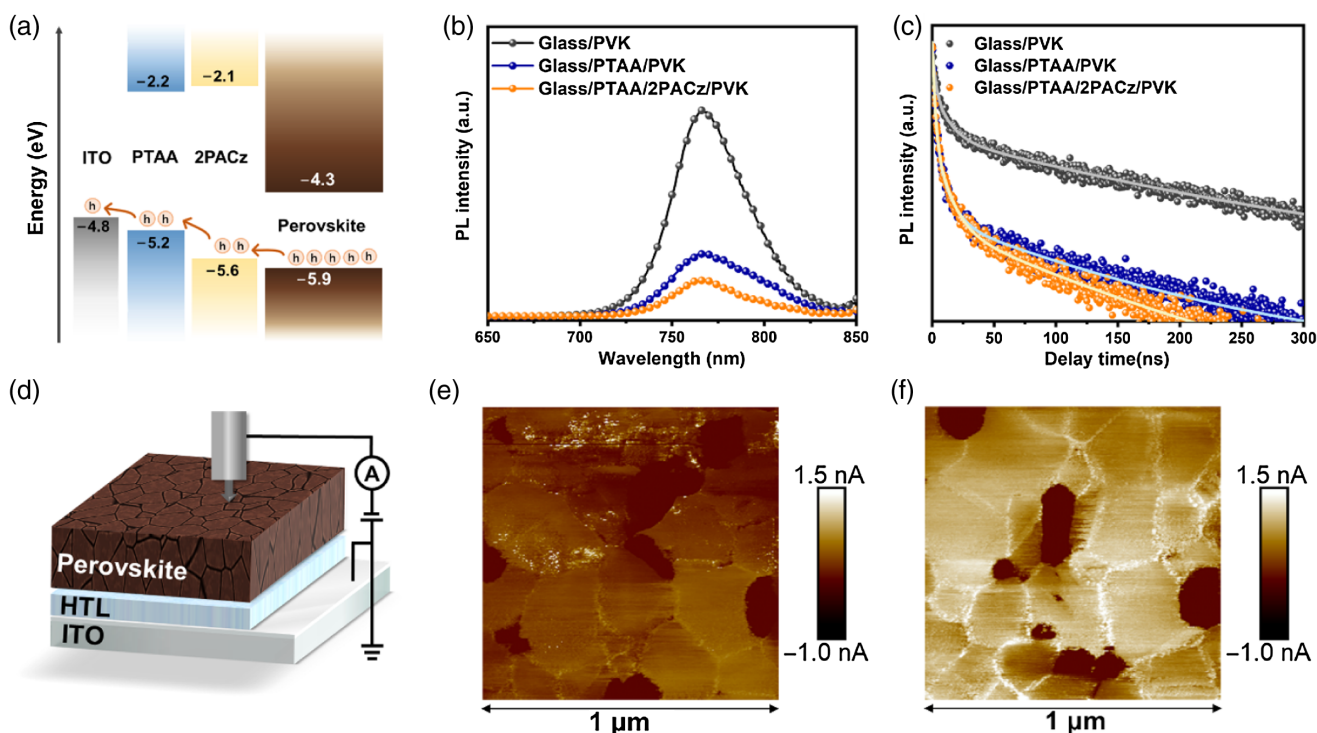


**Figure 3 |** (a) Schematics of energy level diagram of ITO, PTAA, 2PACz, and  $Cs_{0.05}(FA_{0.83}MA_{0.17})_{0.95}Pb(I_{0.83}Br_{0.17})_3$  perovskites. (b) PL and (c) TRPL spectra of glass/perovskite (PVK), glass/PTAA/PVK and glass/PTAA/2PACz/PVK films. (d) The device structure and setup for c-AFM measurement. The local dark-current of the devices with the structure of (e) ITO/PTAA/perovskite and (f) ITO/PTAA/2PACz/perovskite.

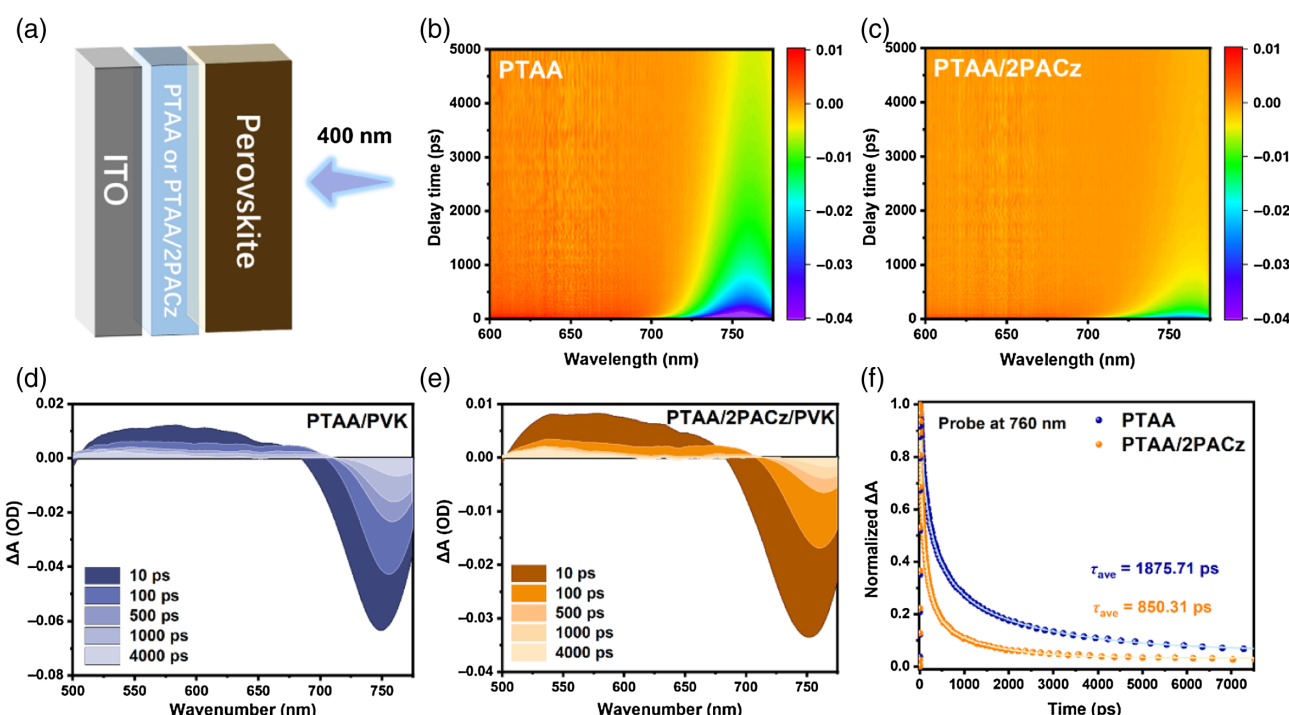


**Figure 4 |** (a) Schematic illustration of the device architecture for TA measurement. Contour plots and delay time-dependent TA spectra of the (b, d) ITO/PTAA/perovskite and (c, e) ITO/PTAA/2PACz/perovskite films. (f) Dynamic TA decay probed at the GSB peak for the samples with or without 2PACz.

DOI: 10.31635/ccschem.022.202202154

Citation: CCS Chem. 2023, 5, 1802–1814

Link to VoR: <https://doi.org/10.31635/ccschem.022.202202154>

(Figure 4b,c). The GSB peak intensity changes with the delay time, which can directly reflect the photoinduced carrier population in the conduction band and valence band of perovskite.<sup>61</sup> In general, the GSB peak decayed more significantly when the delay time was prolonged. For the perovskite film deposited on PTAA/2PACz HTL, the GSB peak intensity at the same delay time appeared to be much weaker, as compared to its control PTAA HTL-based counterpart (Figure 4d,e). The delay kinetics of GSB were analyzed and interpreted via triple-exponential fitting. A much faster TA decay was observed for the sample with 2PACz modification (i.e., 850.31 vs 1875.71 ps, Figure 4f and Supporting Information Table S3), once again confirming the accelerated charge extraction from the interfacially passivated perovskite layer to 2PACz-functionalized PTAA HTL.<sup>62</sup> Overall, the optimized interfacial carrier dynamics, that is, maximized charge extraction and minimized charge recombination at HTL/perovskite interface, greatly contributed to reduce the interfacial energy loss and series resistance, which is conducive to improving  $J_{SC}$  and FF, thus resulting in desirable promotion of device performance in inverted PSCs.

The perovskite materials and devices are very sensitive and can easily degrade under continuous exposure to moisture, heat, oxygen, or light. Such harmful degradation is usually triggered at the active defective sites, such as the grain boundaries and surface of perovskites, as well as their relevant interfaces with other functional layers.<sup>63</sup> In addition to pursuing higher efficiency, the long-term stability of PSCs should be also considered and enhanced for the practical deployment of perovskite photovoltaics. In order to reveal the influence of 2PACz modification layer on device stability, we traced the long-term stability of the unencapsulated devices upon storage in ambient conditions (relative humidity of ~30%–60%) or heating at 85 °C. Encouragingly, there is almost no PCE loss accompanied by negligible decrease of  $J_{SC}$  and FF for the device with 2PACz interfacial modification after 2000 h storage in ambient condition, which is superior to that of the PTAA-based device (Figure 5a and Supporting Information Figure S16). Continuous thermal stress over 60 °C will inevitably incur perovskite composition segregation (i.e. metal halides precipitation and organic component evaporation) and cause device performance degradation.<sup>64</sup> We thus investigated the thermal stability of resultant

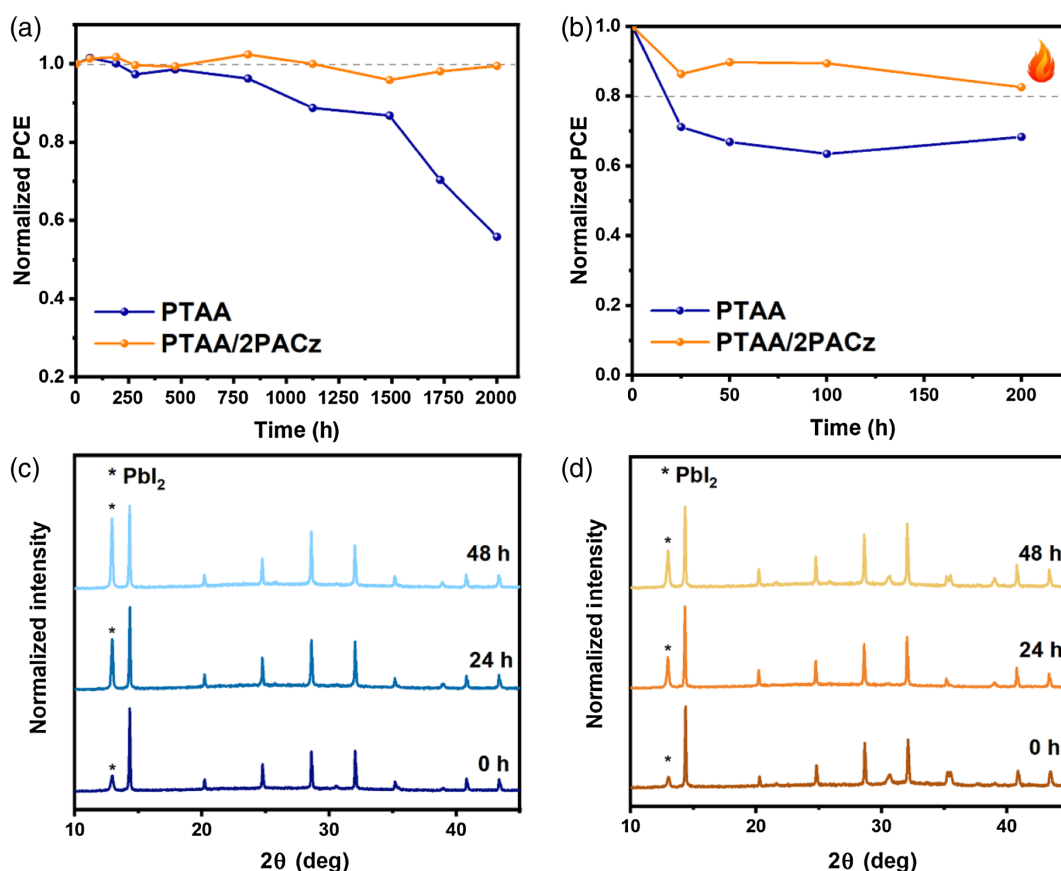


**Figure 5 |** PCE evolution as a function of time for the unencapsulated devices (a) in ambient air and (b) under continuous heating at 85 °C. Change of XRD patterns of the perovskite films deposited on (c) PTAA and (d) PTAA/2PACz HTL upon 85 °C heating for different duration.

PSCs based on different HTLs. As a result, the PTAA/2PACz-based devices retained over 82% of initial PCEs after 200 h of continuous heating at 85 °C, while only 68% of the initial PCEs was retained for the control devices (Figure 5b). The enhanced thermal stability can be attributed to retarded precipitation of  $\text{PbI}_2$  from the perovskite in the presence of 2PACz interfacial locker (Figure 5c,d), highlighting the significance of interfacial linkage and chemical bonding to making more thermally stable PSCs.

## Conclusion

We demonstrated the multifaceted functions of 2PACz molecules when served as an interfacial linker and passivator in *p-i-n* structured PSCs. Simply modifying the PTAA surface with 2PACz perfectly tackling the dilemma of poor wettability to the perovskite ink and underoptimized the energy level alignment with adjacent contacts, regardless of the perovskite compositions. 2PACz-assisted interfacial modification enabled expedited hole extraction, robust interfacial and bulk defect passivation, and well-suppressed charge recombination at the buried HTL/perovskite interface. The blade-coated PSCs achieved a champion PCE of 22.23%, accompanied by negligible hysteresis and excellent reproducibility, which represented one of the highest reported values for the bilayered HTL-based inverted PSCs (Supporting Information Table S4). 2PACz can serve as an efficient molecular hinge to lock the metal halides and suppress the composition segregation under thermal stress, which remarkably enhance the thermal stability of PTAA-based devices with 2PACz modification. This work elucidates the importance of optimizing the interfacial contact properties and carrier dynamics of PSCs, providing a general approach to enhance the efficiency and stability of inverted PSCs that can offer boundless prospects in the commercialization of perovskite photovoltaics or other optoelectronic applications.

## Supporting Information

Supporting Information is available and includes SEM images, AFM topography images, Raman spectra, contact angle images, XRD patterns, SCLC result, EIS spectra, fitting parameters for TRPL and TA measurement, EQE spectra, *J-V* hysteresis, and stability data on the devices.

## Conflict of Interest

The authors declare no competing financial interest.

## Acknowledgments

The authors acknowledge the financial support from the National Natural Science Foundation of China (grant no.

22005355), the Guangdong Basic and Applied Basic Research Foundation (grant no. 2022A1515010282), and the Fundamental Research Funds for the Central Universities, Sun Yat-sen University (grant no. 22qntd2305).

## References

- Lee, M. M.; Teuscher, J.; Miyasaka, T.; Murakami, T. N.; Snaith, H. J. Efficient Hybrid Solar Cells Based on Meso-Superstructured Organometal Halide Perovskites. *Science* **2012**, *338*, 643–647.
- Stranks, S. D.; Eperon, G. E.; Grancini, G.; Menelaou, C.; Alcocer, M. J. P.; Leijtens, T.; Herz, L. M.; Petrozza, A.; Snaith, H. J. Electron-Hole Diffusion Lengths Exceeding 1 Micrometer in an Organometal Trihalide Perovskite Absorber. *Science* **2013**, *342*, 341–344.
- Jeon, N. J.; Noh, J. H.; Kim, Y. C.; Yang, W. S.; Ryu, S.; Seok, S. I. Solvent Engineering for High-Performance Inorganic–Organic Hybrid Perovskite Solar Cells. *Nat. Mater.* **2014**, *13*, 897–903.
- Dong, Q.; Fang, Y.; Shao, Y.; Mulligan, P.; Qiu, J.; Cao, L.; Huang, J. Electron-Hole Diffusion Lengths > 175 μm in Solution-Grown  $\text{CH}_3\text{NH}_3\text{PbI}_3$  Single Crystals. *Science* **2015**, *347*, 967–970.
- NATIONAL RENEWABLE ENERGY LABORATORY (NREL). Best Research-Cell Efficiencies. <https://www.nrel.gov/pv/cell-efficiency.html> (accessed May 2022).
- Ru, P.; Bi, E.; Zhang, Y.; Wang, Y.; Kong, W.; Sha, Y.; Tang, W.; Zhang, P.; Wu, Y.; Chen, W.; Yang, X.; Chen, H.; Han, L. High Electron Affinity Enables Fast Hole Extraction for Efficient Flexible Inverted Perovskite Solar Cells. *Adv. Energy Mater.* **2020**, *10*, 1903487.
- Yu, Z.; Chen, X.; Harvey, S. P.; Ni, Z.; Chen, B.; Chen, S.; Yao, C.; Xiao, X.; Xu, S.; Yang, G.; Yan, Y.; Berry, J. J.; Beard, M. C.; Huang, J. Gradient Doping in Sn-Pb Perovskites by Barium Ions for Efficient Single-Junction and Tandem Solar Cells. *Adv. Mater.* **2022**, *34*, 2110351.
- Li, Z.; Li, B.; Wu, X.; Sheppard, S. A.; Zhang, S.; Gao, D.; Long, N. J.; Zhuo, Z. Organometallic-Functionalized Interfaces for Highly Efficient Inverted Perovskite Solar Cells. *Science* **2022**, *376*, 416–420.
- Li, X.; Zhang, W.; Guo, X.; Lu, C.; Wei, J.; Fang, J. Constructing Heterojunctions by Surface Sulfidation for Efficient Inverted Perovskite Solar Cells. *Science* **2022**, *375*, 434–437.
- Chen, H.; Teale, S.; Chen, B.; Hou, Y.; Grater, L.; Zhu, T.; Bertens, K.; Park, S. M.; Atapattu, H. R.; Gao, Y.; Wei, M.; Johnston, A. K.; Zhou, Q.; Xu, K.; Yu, D.; Han, C.; Cui, T.; Jung, E. H.; Zhou, C.; Zhou, W.; Proppe, A. H.; Hoogland, S.; Laquai, F.; Filletter, T.; Graham, K. R.; Ning, Z.; Sargent, E. H. Quantum-Size-Tuned Heterostructures Enable Efficient and Stable Inverted Perovskite Solar Cells. *Nat. Photon.* **2022**, *16*, 352–358.
- Azmi, R.; Ugur, E.; Seitkhan, A.; Aljamaan, F.; Subbiah, A. S.; Li, J.; Harrison, G. T.; Nugraha, M. I.; Eswaran, M. K.; Babics, M.; Chen, Y.; Xu, F.; Allen, T. G.; Rehman, A. U.; Wang, C.-L.; Anthopoulos, T. D.; Schwingenschlögl, U.; Bastiani, M. D.; Aydin, E.; Wolf, S. D. Damp Heat-Stable Perovskite Solar

- Cells with Tailored-Dimensionality 2D/3D Heterojunctions. *Science* **2022**, *376*, 73–77.
12. Liu, X.; Cheng, Y.; Liu, C.; Zhang, T.; Zhang, N.; Chen, J.; Xu, Q.; Ouyang, J.; Gong, H. 20.7% Highly Reproducible Inverted Planar Perovskite Solar Cells with Enhanced Fill Factor and Eliminated Hysteresis. *Energy Environ. Sci.* **2019**, *12*, 1622–1633.
13. Ni, Z.; Bao, C.; Liu, Y.; Jiang, Q.; Wu, W.-Q.; Chen, S.; Dai, X.; Chen, B.; Hartweg, B.; Yu, Z.; Holman, Z.; Huang, J. Resolving Spatial and Energetic Distributions of Trap States in Metal Halide Perovskite Solar Cells. *Science* **2020**, *367*, 1352–1358.
14. Khan, J. I.; Isikgor, F. H.; Ugur, E.; Raja, W.; Harrison, G. T.; Yengel, E.; Anthopoulos, T. D.; Wolf, S. D.; Laquai, F. Charge Carrier Recombination at Perovskite/Hole Transport Layer Interfaces Monitored by Time-Resolved Spectroscopy. *ACS Energy Lett.* **2021**, *6*, 4155–4164.
15. Luo, D.; Yang, W.; Wang, Z.; Sadhanala, A.; Hu, Q.; Su, R.; Shivanna, R.; Trindade, G. F.; Watts, J. F.; Xu, Z.; Liu, T.; Chen, K.; Ye, F.; Wu, P.; Zhao, L.; Wu, J.; Tu, Y.; Zhang, Y.; Yang, X.; Zhang, W.; Friend, R. H.; Gong, Q.; Snaith, H. J.; Zhu, R. Enhanced Photovoltage for Inverted Planar Heterojunction Perovskite Solar Cells. *Science* **2018**, *360*, 1442–1446.
16. Jung, E. D.; Harit, A. K.; Kim, D. H.; Jang, C. H.; Park, J. H.; Cho, S.; Song, M. H.; Woo, H. Y. Multiply Charged Conjugated Polyelectrolytes as a Multifunctional Interlayer for Efficient and Scalable Perovskite Solar Cells. *Adv. Mater.* **2020**, *32*, 2002333.
17. Xu, X.; Ji, X.; Chen, R.; Ye, F.; Liu, S.; Zhang, S.; Chen, W.; Wu, Y.; Zhu, W.-H. Improving Contact and Passivation of Buried Interface for High-Efficiency and Large-Area Inverted Perovskite Solar Cells. *Adv. Funct. Mater.* **2022**, *32*, 2109968.
18. Sun, Q.; Zong, B.; Meng, X.; Shen, B.; Li, X.; Kang, B.; Silva, S. R. P. Interface Regulation by an Ultrathin Wide-Bandgap Halide for Stable and Efficient Inverted Perovskite Solar Cells. *ACS Appl. Mater. Interfaces* **2022**, *14*, 6702–6713.
19. Li, Y.; Wang, B.; Liu, T.; Zeng, Q.; Cao, D.; Pan, H.; Xing, G. Interfacial Engineering of PTAA/Perovskites for Improved Crystallinity and Hole Extraction in Inverted Perovskite Solar Cells. *ACS Appl. Mater. Interfaces* **2022**, *14*, 3284–3292.
20. Wang, Q.; Bi, C.; Huang, J. Doped Hole Transport Layer for Efficiency Enhancement in Planar Heterojunction Organolead Trihalide Perovskite Solar Cells. *Nano Energy* **2015**, *15*, 275–280.
21. Kim, Y.; Jung, E. H.; Kim, G.; Kim, D.; Kim, B. J.; Seo, J. Sequentially Fluorinated PTAA Polymers for Enhancing  $V_{OC}$  of High-Performance Perovskite Solar Cells. *Adv. Energy Mater.* **2018**, *8*, 1801668.
22. Xu, G.; Xue, R.; Stuard, S. J.; Ade, H.; Zhang, C.; Yao, J.; Li, Y.; Li, Y. Reducing Energy Disorder of Hole Transport Layer by Charge Transfer Complex for High Performance  $p-i-n$  Perovskite Solar Cells. *Adv. Mater.* **2021**, *33*, 200675.
23. Wang, H.; Song, Y.; Kang, Y.; Dang, S.; Feng, J.; Dong, Q. Reducing Photovoltage Loss at the Anode Contact of Methylammonium-Free Inverted Perovskite Solar Cells by Conjugated Polyelectrolyte Doping. *J. Mater. Chem. A* **2020**, *8*, 7309–7316.
24. Barard, S.; Heeney, M.; Chen, L.; Cölle, M.; Shkunov, M.; McCulloch, I.; Stingelin, N.; Philips, M.; Kreouzis, T. Separate Charge Transport Pathways Determined by the Time of Flight Method in Bimodal Polytriarylamine. *J. Appl. Phys.* **2009**, *105*, 013701.
25. Rombach, F. M.; Haque, S. A.; Macdonald, T. J. Lessons Learned from Spiro-OMeTAD and PTAA in Perovskite Solar Cells. *Energy Environ. Sci.* **2021**, *14*, 5161–5190.
26. Zhang, L.; Zhou, X.; Zhong, X.; Cheng, C.; Tian, Y.; Xu, B. Hole-Transporting Layer Based on a Conjugated Polyelectrolyte with Organic Cations Enables Efficient Inverted Perovskite Solar Cells. *Nano Energy* **2019**, *57*, 248–255.
27. Zhou, Q.; Qiu, J.; Wang, Y.; Yu, M.; Liu, J.; Zhang, X. Multifunctional Chemical Bridge and Defect Passivation for Highly Efficient Inverted Perovskite Solar Cells. *ACS Energy Lett.* **2021**, *6*, 1596–1606.
28. Hu, X.; Meng, X.; Zhang, L.; Zhang, Y.; Cai, Z.; Huang, Z.; Su, M.; Wang, Y.; Li, M.; Li, F.; Yao, X.; Wang, F.; Ma, W.; Chen, Y.; Song, Y. A Mechanically Robust Conducting Polymer Network Electrode for Efficient Flexible Perovskite Solar Cells. *Joule* **2019**, *3*, 2205–2218.
29. Yao, Z.; Zhang, F.; Guo, Y.; Wu, H.; He, L.; Liu, Z.; Cai, B.; Guo, Y.; Brett, C. J.; Li, Y.; Srambickal, C. V.; Yang, X.; Chen, G.; Widengren, J.; Liu, D.; Gardner, J. M.; Kloo, L.; Sun, L., Conformational and Compositional Tuning of Phenanthrocarbazole-Based Dopant-Free Hole-Transport Polymers Boosting the Performance of Perovskite Solar Cells. *J. Am. Chem. Soc.* **2020**, *142*, 17681–17692.
30. Al-Ashouri, A.; Magomedov, A.; Roß, M.; Jošt, M.; Talaiakis, M.; Chistiakova, G.; Bertram, T.; Márquez, J. A.; Köhnen, E.; Kasparavicius, E.; Levchenko, S.; Gil-Escríg, L.; Hages, C. J.; Schlatmann, R.; Rech, B.; Malinauskas, T.; Unold, T.; Kauffmann, C. A.; Korte, L.; Niaura, G.; Getautis, V.; Albrecht, S. Conformal Monolayer Contacts with Lossless Interfaces for Perovskite Single Junction and Monolithic Tandem Solar Cells. *Energy Environ. Sci.* **2019**, *12*, 3356–3369.
31. Al-Ashouri, A.; Köhnen, E.; Li, B.; Magomedov, A.; Hempel, H.; Caprioglio, P.; Márquez, J. A.; Vilches, A. B. M.; Kasparavicius, E.; Smith, J. A.; Phung, N.; Menzel, D.; Grischek, M.; Kegelmann, L.; Skroblin, D.; Gollwitzer, C.; Malinauskas, T.; Jošt, M.; Matič, G.; Rech, B.; Schlatmann, R.; Topic, M.; Korte, L.; Abate, A.; Stannowski, B.; Neher, D.; Stolterfoht, M.; Unold, T.; Getautis, V.; Albrecht, S. Conformal Monolayer Contacts with Lossless Interfaces for Perovskite Single Junction and Monolithic Tandem Solar Cells. *Science* **2020**, *370*, 1300–1309.
32. Lin, Y.; Magomedov, A.; Firdaus, Y.; Kaltsas, D.; El-Labban, A.; Faber, H.; Naphade, D. R.; Yengel, E.; Zheng, X.; Yarali, E.; Chaturvedi, N.; Loganathan, K.; Gkeka, D.; AlShammari, S. H.; Bakr, O. M.; Laquai, F.; Tsetseris, L.; Getautis, V.; Anthopoulos, T. D. 18.4% Organic Solar Cells Using a High Ionization Energy Self-Assembled Monolayer as Hole-Extraction Interlayer. *ChemSusChem* **2021**, *14*, 3569–3578.
33. Heo, J. H.; You, M. S.; Chang, M. H.; Yin, W.; Ahn, T. K.; Lee, S.-J.; Sung, S.-J.; Kim, D. H.; Im, S. H. Hysteresis-Less Mesoscopic  $\text{CH}_3\text{NH}_3\text{PbI}_3$  Perovskite Hybrid Solar Cells by

- Introduction of Li-Treated TiO<sub>2</sub> Electrode. *Nano Energy* **2015**, *15*, 530–539.
34. Cui, B.-B.; Yang, N.; Shi, C.; Yang, S.; Shao, J.-Y.; Han, Y.; Zhang, L.; Zhang, Q.; Zhong, Y.-W.; Chen, Q. Naphtho[1,2-b:4,3-b']dithiophene-Based Hole Transporting Materials for High-Performance Perovskite Solar Cells: Molecular Engineering and Opto-Electronic Properties. *J. Mater. Chem. A* **2018**, *6*, 10057–10063.
35. Xie, H.; Wang, Z.; Chen, Z.; Pereyra, C.; Pols, M.; Gałkowski, K.; Anaya, M.; Fu, S.; Jia, X.; Tang, P.; Kubicki, D. J.; Agarwalla, A.; Kim, H.-S.; Prochowicz, D.; Borrisé, X.; Bonn, M.; Bao, C.; Sun, X.; Zakeeruddin, S. M.; Emsley, L.; Arbiol, J.; Gao, F.; Fu, F.; Wang, H. I.; Tielrooij, K.-J.; Stranks, S. D.; Tao, S.; Grätzel, M.; Hagfeldt, A.; Lira-Cantu, M. Decoupling the Effects of Defects on Efficiency and Stability through Phosphonates in Stable Halide Perovskite Solar Cells. *Joule* **2021**, *5*, 1246–1266.
36. Li, X.; Ibrahim Dar, M.; Yi, C.; Luo, J.; Tschumi, M.; Zakeeruddin, S. M.; Nazeeruddin, M. K.; Han, H.; Grätzel, M. Improved Performance and Stability of Perovskite Solar Cells by Crystal Crosslinking with Alkylphosphonic Acid  $\omega$ -Ammonium Chlorides. *Nat. Chem.* **2015**, *7*, 703–711.
37. Wu, W.-Q.; Yang, Z.; Rudd, P. N.; Shao, Y.; Dai, X.; Wei, H.; Zhao, J.; Fang, Y.; Wang, Q.; Liu, Y.; Deng, Y.; Xiao, X.; Feng, Y.; Huang, J. Bilateral Alkylamine for Suppressing Charge Recombination and Improving Stability in Blade-Coated Perovskite Solar Cells. *Sci. Adv.* **2019**, *5*, eaav8925.
38. Li, M.; Zhao, Y.; Qin, X.; Ma, Q.; Lu, J.; Lin, K.; Xu, P.; Li, Y.; Feng, W.; Zhang, W.-H.; Wei, Z. Conductive Phosphine Oxide Passivator Enables Efficient Perovskite Light-Emitting Diodes. *Nano Lett.* **2022**, *22*, 2490–2496.
39. Qiu, X.; Liu, Y.; Li, W.; Hu, Y. Traps in Metal Halide Perovskites: Characterization and Passivation. *Nanoscale* **2020**, *12*, 22425–22451.
40. Liu, T.; Chen, K.; Hu, Q.; Zhu, R.; Gong, Q. Inverted Perovskite Solar Cells: Progresses and Perspectives. *Adv. Energy Mater.* **2016**, *6*, 1600457.
41. Zhang, F.; Zhu, K. Additive Engineering for Efficient and Stable Perovskite Solar Cells. *Adv. Energy Mater.* **2020**, *10*, 1902579.
42. Bi, C.; Wang, Q.; Shao, Y.; Yuan, Y.; Xiao, Z.; Huang, J. Non-Wetting Surface-Driven High-Aspect-Ratio Crystalline Grain Growth for Efficient Hybrid Perovskite Solar Cells. *Nat. Commun.* **2015**, *6*, 7747.
43. Chen, J.; Park, N.-G. Materials and Methods for Interface Engineering toward Stable and Efficient Perovskite Solar Cells. *ACS Energy Lett.* **2020**, *5*, 2742–2786.
44. Wang, Y.; Ju, H.; Mahmoudi, T.; Liu, C.; Zhang, C.; Wu, S.; Yang, Y.; Wang, Z.; Hu, J.; Cao, Y.; Guo, F.; Hahn, Y.-B.; Mai, Y. Cation-Size Mismatch and Interface Stabilization for Efficient NiOx-Based Inverted Perovskite Solar Cells with 21.9% Efficiency. *Nano Energy* **2021**, *88*, 106285.
45. Yang, J.; Liu, C.; Cai, C.; Hu, X.; Huang, Z.; Duan, X.; Meng, X.; Yuan, Z.; Tan, L.; Chen, Y. High-Performance Perovskite Solar Cells with Excellent Humidity and Thermo-Stability via Fluorinated Perylenediimide. *Adv. Energy Mater.* **2019**, *9*, 1900198.
46. Zhang, Y.; Liu, X.; Li, P.; Duan, Y.; Hu, X.; Li, F.; Song, Y. Dopamine-Crosslinked TiO<sub>2</sub>/Perovskite Layer for Efficient and Photostable Perovskite Solar Cells under Full Spectral Continuous Illumination. *Nano Energy* **2019**, *56*, 733–740.
47. Chen, S.; Dai, X.; Xu, S.; Jiao, H.; Zhao, L.; Huang, J. Stabilizing Perovskite-Substrate Interfaces for High-Performance Perovskite Modules. *Science* **2021**, *373*, 902–907.
48. Cao, J.; Loi, H.-L.; Xu, Y.; Guo, X.; Wang, N.; Liu, C.-K.; Wang, T.; Cheng, H.; Zhu, Y.; Li, M.G.; Wong, W.-Y.; Yan, F. High-Performance Tin-Lead Mixed-Perovskite Solar Cells with Vertical Compositional Gradient. *Adv. Mater.* **2022**, *34*, 2107729.
49. Zheng, X.; Hou, Y.; Bao, C.; Yin, J.; Yuan, F.; Huang, Z.; Song, K.; Liu, J.; Troughton, J.; Gasparini, N.; Zhou, C.; Lin, Y.; Xue, D.-J.; Chen, B.; Johnston, A. K.; Wei, N.; Hedhili, M. N.; Wei, M.; Alsalloum, A. Y.; Maity, P.; Turedi, B.; Yang, C.; Baran, D.; Anthopoulos, T. D.; Han, Y.; Lu, Z.-H.; Mohammed, O. F.; Gao, F.; Sargent, E. H.; Bakr, O. M. Managing Grains and Interfaces via Ligand Anchoring Enables 22.3%-Efficiency Inverted Perovskite Solar Cells. *Nat. Energy* **2020**, *5*, 131–140.
50. Zhang, J.; Fang, Y.; Zhao, W.; Han, R.; Wen, J.; Liu, S. (F.) Molten-Salt-Assisted CsPbI<sub>3</sub> Perovskite Crystallization for Nearly 20%-Efficiency Solar Cells. *Adv. Mater.* **2021**, *33*, 2103770.
51. Lin, R.; Xiao, K.; Qin, Z.; Han, Q.; Zhang, C.; Wei, M.; Saidaminov, M. I.; Gao, Y.; Xu, J.; Xiao, M.; Li, A.; Zhu, J.; Sargent, E. H.; Tan, H. Monolithic All-Perovskite Tandem Solar Cells with 24.8% Efficiency Exploiting Comproportionation to Suppress Sn(II) Oxidation in Precursor ink. *Nat. Energy* **2019**, *4*, 864–873.
52. Wu, S.; Zhang, J.; Li, Z.; Liu, D.; Qin, M.; Cheung, S. H.; Lu, X.; Lei, D.; So, S. K.; Zhu, Z.; Jen, A.-Y. Modulation of Defects and Interfaces through Alkylammonium Interlayer for Efficient Inverted Perovskite Solar Cells. *Joule* **2020**, *4*, 1248–1262.
53. Li, G.; Jiang, Y.; Deng, S.; Tam, A.; Xu, P.; Wong, M.; Kwok, H.-S. Overcoming the Limitations of Sputtered Nickel Oxide for High-Efficiency and Large-Area Perovskite Solar Cells. *Adv. Sci.* **2017**, *4*, 1700463.
54. Li, Y.; Xie, H.; Lim, E. L.; Hagfeldt, A.; Bi, D. Recent Progress of Critical Interface Engineering for Highly Efficient and Stable Perovskite Solar Cells. *Adv. Energy Mater.* **2022**, *12*, 2102730.
55. Zhang, Z.; Liang, Y.; Huang, H.; Liu, X.; Li, Q.; Chen, L.; Xu, D. Stable and Highly Efficient Photocatalysis with Lead-Free Double-Perovskite of Cs<sub>2</sub>AgBiBr<sub>6</sub>. *Angew. Chem. Int. Ed.* **2019**, *58*, 7263–7267.
56. Jiang, Q.; Zhang, L.; Wang, H.; Yang, X.; Meng, J.; Liu, H.; Yin, Z.; Wu, J.; Zhang, X.; You, J. Enhanced Electron Extraction Using SnO<sub>2</sub> for High-Efficiency Planar-Structure HC (NH<sub>2</sub>)<sub>2</sub>PbI<sub>3</sub>-Based Perovskite Solar Cells. *Nat. Energy* **2017**, *2*, 16177.
57. Fang, Z.; Meng, X.; Zu, C.; Li, D.; Xiao, Z.; Yi, C.; Wang, M.; Jin, Z.; Yang, S.; Ding, L. Interface Engineering Gifts CsPbI<sub>2.25</sub>Br<sub>0.75</sub> Solar Cells High Performance. *Sci. Bull.* **2019**, *64*, 1743–1746.

58. Wang, Q.; Dong, Q.; Li, T.; Gruverman, A.; Huang, J. Thin Insulating Tunneling Contacts for Efficient and Water-Resistant Perovskite Solar Cells. *Adv. Mater.* **2016**, *28*, 6734–6739.
59. Li, B.; Yang, K.; Liao, Q.; Wang, Y.; Su, M.; Li, Y.; Shi, Y.; Feng, X.; Huang, J.; Sun, H.; Guo, X. Imide-Functionalized Triarylamine-Based Donor-Acceptor Polymers as Hole Transporting Layers for High-Performance Inverted Perovskite Solar Cells. *Adv. Funct. Mater.* **2021**, *31*, 2100332.
60. Wu, W.-Q.; Liao, J.-F.; Zhong, J.-X.; Xu, Y.-F.; Wang, L.; Huang, J. Suppressing Interfacial Charge Recombination in Electron-Transport-Layer-Free Perovskite Solar Cells to Give an Efficiency Exceeding 21%. *Angew. Chem.* **2020**, *132*, 21166.
61. Tress, W. Perovskite Solar Cells on the Way to Their Radiative Efficiency Limit—Insights into a Success Story of High Open-Circuit Voltage and Low Recombination. *Adv. Energy Mater.* **2017**, *7*, 1602358.
62. Wu, W.-Q.; Zhong, J.-X.; Liao, J.-F.; Zhang, C.; Zhou, Y.; Feng, W.; Ding, L.; Wang, L.; Kuang, D.-B. Spontaneous Surface/Interface Ligand-Anchored Functionalization for Extremely High Fill Factor over 86% in Perovskite Solar Cells. *Nano Energy* **2020**, *75*, 104929.
63. Roose, B.; Wang, Q.; Abate, A. The Role of Charge Selective Contacts in Perovskite Solar Cell Stability. *Adv. Energy Mater.* **2019**, *9*, 1803140.
64. Yang, J.; Liu, X.; Zhang, Y.; Zheng, X.; He, X.; Wang, H.; Yue, F.; Braun, S.; Chen, J.; Xu, J.; Li, Y.; Jin, Y.; Tang, J.; Duan, C.; Fahlman, M.; Bao, Q. Comprehensive Understanding of Heat-Induced Degradation of Triple-Cation Mixed halide Perovskite for a Robust Solar Cell. *Nano Energy* **2018**, *54*, 218–226.